JOURNAL OF PROPULSION AND POWER
Vol. 24, No. 4, July–August 2008

Wear Mechanisms in Electron Sources for Ion Propulsion, 2: Discharge Hollow Cathode

Ioannis G. Mikellides,* Ira Katz,† Dan M. Goebel,‡ Kristina K. Jameson,§ and James E. Polk¶
Jet Propulsion Laboratory, California Institute of Technology, Pasadena, California 91109

DOI: 10.2514/1.33462

The wear of the keeper electrode in discharge hollow cathodes is a major impediment to the implementation of ion propulsion onboard long-duration space science missions. The development of a predictive theoretical model for hollow cathode keeper life has long been sought, but its realization has been hindered by the complexities associated with the physics of the partially ionized gas and the associated erosion mechanisms in these devices. Thus, although several wear mechanisms have been hypothesized, a quantitative explanation of life test erosion profiles has remained incomplete. A two-dimensional model of the partially ionized gas in a discharge cathode has been developed and applied to understand the mechanisms that drove the erosion of the keeper in two long-duration life tests of a 30-cm ion thruster. An extensive set of comparisons between predictions by the numerical simulations and measurements of the plasma properties and of the erosion patterns is presented. It is found that the near-plume plasma oscillations, predicted by theory and observed by experiment, effectively enhance the resistivity of the plasma as well as the energy of ions striking the keeper.

Nomenclature

A	=	amplitude factor of turbulent oscillation
AW	=	atomic weight
$\mathbf{B}$	=	magnetic field, T
C_s	=	ion acoustic speed, m/s
$\mathbf{E}$	=	electric field, V/m
E_c	=	Dreicer critical field, V/m
E_D	=	Dreicer field, V/m
e	=	electron charge, C
I_d	=	discharge current, A
$\mathbf{j}_e$	=	electron current density, A/m^2
$j_{e,\mathrm{th}}$	=	electron thermal current density, A/m^2
$\mathbf{j}_i$	=	ion current density, A/m^2
k	=	wave number, m^{-1}
k_B	=	Boltzmann's constant, J/K
$\ln\Lambda$	=	Coulomb logarithm
M	=	mass of xenon ion or atom, kg
m_e	=	mass of electron, kg
N_{AV}	=	Avogadro's number, mol^{-1}
n	=	plasma particle density, particles/m^3
$\hat{\mathbf{n}}$	=	normal unit vector
$\dot{n}$	=	ionization rate for $e + Xe \rightarrow Xe^+$, particles/m^3/s
$\ddot{n}$	=	ionization rate for $e + Xe^+ \rightarrow Xe^{++}$, particles/m^3/s
n_p	=	plasma particle density adjacent to boundary, particles/m^3
p_e	=	electron pressure, Pa
p_i	=	ion pressure, Pa
r_K	=	keeper-orifice inner radius, m
T_e	=	electron temperature, K
T_h	=	heavy species temperature, K
T_i	=	ion temperature, K
T_p	=	electron temperature adjacent to boundary, K
u_d	=	electron-ion relative drift speed, m/s
$\mathbf{u}_e$	=	electron velocity, m/s
$\mathbf{u}_i$	=	ion velocity, m/s
$\mathbf{u}_n$	=	neutral velocity, m/s
$u_{T,e}$	=	electron thermal speed $(2k_BT_e/m_e)^{1/2}$, m/s
V_d	=	discharge voltage, V
V_k	=	keeper voltage, V
Y	=	sputtering yield, atoms/ion
α	=	wave number factor, m^{-1}
Δh	=	erosion depth or height, m
Δt	=	time increment, h
ε_i	=	ion energy, J
ε_0	=	electric permittivity of free space, F/m
η	=	resistivity, Ohm-m
λ_D	=	debye length, m
ν_a	=	anomalous collision frequency, s^{-1}
ν_{ei}	=	electron-ion collision frequency, s^{-1}
ν_{en}	=	electron-neutral collision frequency, s^{-1}
ν_{in}	=	ion-neutral collision frequency, s^{-1}
ρ	=	material mass density, kg/m^3
ϕ	=	plasma potential, V
ϕ_p	=	plasma potential adjacent to boundary, V
Ω_e	=	electron Hall parameter
ω_{pi}	=	ion plasma frequency, rad/s

Presented as Paper 5192 at the 43rd AIAA/ASME/SAE/ASEE Joint Propulsion Conference, Cincinnati Duke Energy Convention Center, Cincinnati, OH, 8–11 July 2007; received 15 July 2007; accepted for publication 5 March 2008.

*Member Technical Staff, Electric Propulsion Group, 4800 Oak Grove Drive, Mail Stop 125-109. Senior Member AIAA.

†Group Supervisor, Electric Propulsion Group, 4800 Oak Grove Drive, Mail Stop 125-109. Senior Member AIAA.

‡Section Staff, Thermal and Propulsion Engineering Section, 4800 Oak Grove Drive, Mail Stop 125-109. Senior Member AIAA.

§Academic Part-Time Staff, Thermal and Propulsion Engineering Section, 4800 Oak Grove Drive, Mail Stop 125-109. Member AIAA.

¶Section Staff, Thermal and Propulsion Engineering Section, 4800 Oak Grove Drive, Mail Stop 125-109. Senior Member AIAA.

I. Introduction

HOLLOW cathodes are employed regularly as electron sources in ion and Hall electric propulsion. A major concern regarding the use of hollow cathodes in long-duration robotic space science missions is the erosion of the keeper electrode. Efforts to understand the keeper erosion intensified after NASA performed two major life tests of a 30-cm ion engine called the Life Demonstration Test (LDT) [1] and the Extended-Life Test (ELT) [2]. Both tests revealed significant wear of the discharge hollow cathode (DHC) keeper. Much of the work on keeper erosion has naturally centered on measurements of high-energy ions and the identification of the mechanisms that produce them. Several such mechanisms have been proposed, including potential hills [3], charge exchange between ions and neutrals [4,5], double ionization [5], triple ionization [6], multiple collisions of ions with the cathode orifice wall [7], magnetohydrodynamic effects [8], and plasma potential oscillations [9]. The proposed mechanisms have been based largely on empirical observations and/or phenomenological models.

The inherent two-dimensional nature of the plasma both inside and outside the cathode limits the ability of zero-dimensional and one-dimensional theoretical models to explain many of the plasma features alluded to in the preceding paragraph. Before the present work, only a few attempts were reported that modeled, in two dimensions, the ionized gas produced by electric propulsion hollow cathodes. Salhi and Turchi [10] developed a first-principles fluid model that included a 2-D variation of the plasma properties, but only inside the cathode. The electron-neutral (*e-n*) and ion-neutral (*i-n*) collisions were excluded. Boyd and Crofton [11] developed a hybrid particle-fluid model to simulate the plasma plume of a low-current (<1.8 A), low-flow (<1 standard cm^3/min) hollow cathode that included all relevant particle collisions. The simulated region included the cathode-to-keeper gap and the keeper-orifice region. At the exit of the cathode the plasma potential was specified to be near the keeper voltage, which ranged from 26 to 34 V with respect to cathode ground (0 V). Thus, with the keeper also serving as the anode, the plasma potential solution naturally exhibited a nonmonotonic profile with distance from the cathode exit due to the resistive drop $\eta \boldsymbol{j}_e$ that is maximized at the keeper orifice. In the Boyd–Crofton cathode setup, the potential *fell* monotonically with distance downstream of the keeper exit. The electric field established in the keeper interior was computed to be relatively benign and could be accounted for by classical Ohm's law in two out of the three cases simulated. By contrast, in the discharge cathode studied here, the anode is the (conical) discharge chamber of the ion thruster, and so the plasma potential typically *rises* monotonically from the cathode interior to the far-plume region [12,13]. For typical ion thruster discharge cathodes, the measurements show that the steepest gradients of the plasma potential occur in the plume region near the keeper, and that the plasma potential at the cathode exit does not exceed ∼15 V with respect to cathode ground. It is precisely these observed high electric field values in the near plume that present the challenge: it has been suggested by the authors, both in this paper and in previous work with a different cathode [14], that due to the loss of classical *e-e* collisions in this near-plume region, the measured rise in the plasma potential cannot be accounted for by the classical resistive drop in the plasma alone. That is, when the main plasma variables (number density, electron temperature, and plasma potential), computed or measured, were substituted into classical Ohm's law, the law could not be completely satisfied in these high-field regions.

The structure of the plasma potential in the keeper region is of particular interest because it may also be directly associated with the attainable ion energies. In a few of the studies cited previously, it has been sufficient to regard the spatial or temporal profiles of the plasma potential obtained by the measurements as de facto for the purpose of establishing hypotheses on the generation mechanism(s) and direction of high-energy ions. The details of how and why the discharge establishes a spatially rising plasma potential downstream of the keeper while in some cases exhibiting high-amplitude temporal fluctuations, or the reason(s) for the absence of a nonmonotonic profile (potential hill), have not yet been fully identified and explained. Moreover, the mechanism(s) that heat the relatively cold ($k_B T_e = 1$–2 eV) electrons inside the cathode to temperatures that in some cases exceed 5 eV in the near-plume region has not been rigorously identified. Nonetheless, some studies have shown how the proposed mechanism(s) could have formed the shape of the erosion that was observed along the keeper surface during the life tests [5]. In the present work, we present an extensive set of comparisons between numerical simulation results and plasma measurements in the near plume, offer explanations of the observed trends based on these comparisons, and provide predictions of both the shape and magnitude of the erosion.

Two 2-D computational models of the hollow cathode have been developed by the authors of this paper. The first model [15] was developed to simulate the emitter region of the hollow cathode. Upon the completion of the model, it was proposed that anomalous heating by ion acoustic turbulence (IAT) was possible in view of the elevated temperatures observed inside the orifice and near-plume regions of a 1.5-cm, 25-A DHC. The second 2-D model [16] was developed to allow for the global simulation of the cathode plasma by extending both the conservation laws and the computational region. Recently this model was applied to determine the erosion of the orifice channel in a neutralizer hollow cathode (NHC) [17]. The numerical simulations showed that the acceleration of singly charged xenon ions by the sheath was sufficient to explain the observed erosion of the orifice. No additional mechanisms beyond this classical picture were found necessary. By extensive numerical simulation it is shown in this paper that the same classical mechanism—ion acceleration by the sheath—remains the fundamental mechanism for the erosion of the keeper. But, in contrast to the NHC, the magnitude of the sheath drop is shown to be effectively enhanced by the adjacent low-frequency (<500 kHz) plasma pulsations that occur naturally in the discharge.

II. Discharge Hollow Cathode: Basic Description of the Device and Related Data

The main components of a hollow cathode used in the two life tests have been presented in a companion paper [17]. Two operating points of the ion engine will be of interest in this article, full-power operating condition (TH15) and lower-power level (TH8). Tables 1 and 2 provide basic geometrical and operational characteristics of the DHC in the 30-cm ion thruster.

Photographs of the discharge cathodes after the completion of the two tests are shown in Figs. 1 and 2. The LDT DHC was operated at TH15. The erosion pattern of the keeper plate surface facing the cathode plume is shown in Fig. 1. After 8200 h of operation, the erosion of the surface exhibited a curved pattern with a maximum erosion depth of about 500 μm. Direct comparisons between the eroded profile and predictions from the numerical simulations are the subject of Sec. IV.B.1. The ELT DHC keeper was completely eroded by the end of the test. The evolution of the keeper-orifice channel erosion has been determined from photographs of the keeper plate taken at various times during the ELT (Fig. 2). In Sec. IV.B.2, the observed opening of the channel is compared with predictions from the numerical simulations. Of particular interest in the ELT is the accelerated erosion of the keeper orifice that began after ∼8000 h of operation as shown in Fig. 3. Two events distinguish the ELT from the LDT during this operation segment. First, the ELT cathode was operated at TH8, and second, the cathode-to-keeper (C–K) voltage

Table 1 Typical operational characteristics of the 30-cm ion engine discharge hollow cathode

Operational characteristics	TH15	TH8
Discharge current, A	13.3	8.24
Discharge voltage, V	25.6	26.3
Mass flow rate, sccm	3.7	2.47
Peak emitter temperature,[a] K	1473	1383

[a]Emitter temperatures were not measured during the life tests. The values are based on measurements taken later during the testing of individual cathodes [43].

Table 2 Typical geometrical characteristics of the 30-cm ion engine discharge hollow cathode

Geometrical characteristics	
Cathode tube diameter, cm	0.635
Cathode orifice radius, cm	0.051
Keeper-orifice (inner) radius, cm	0.237
Orifice (cyl) channel length, cm	0.074
Emitter insert length, cm	2.54
Orifice plate material	Tungsten (W)
Keeper plate material	Molybdenum (Mo)

was shorted, causing the keeper voltage to drop by about 3 V. The short occurred at 5850 h and was cleared at 8873 h [18]. Using a surface layer activation technique and an accelerated test (with operation time <100 h), Kolasinski et al. [19] showed by direct measurement that a 2.8 V reduction of the keeper voltage increased the erosion rate by almost 65% in the keeper orifice. The work also concluded that chamfering of the orifice likely occurred during the ELT, in agreement with the observed chamfering seen in the LDT (see Fig. 1, left). However, the plasma properties near the eroding surface and, in turn, the erosion of surface itself changed as a result of the chamfering, and this effect could not be taken into account in the accelerated test. The significance of the altered plasma properties due to the chamfering of the keeper channel is quantified and discussed in Sec. IV.B.2.

It is widely accepted that erosion of these cathodes occurs as a result of surface sputtering by ion bombardment. The sputtering yield as a function of xenon ion energy has been measured by Doerner et al. for molybdenum (Mo) [20] and for tantalum (Ta) [21] for values as low as 15 V. The measurements have been fitted with general functions, and the fits are used in the erosion calculations of Sec. IV.B. An extrapolation to the measurements is used for ion energies below 15 V. The fitted data are shown in Fig. 4.

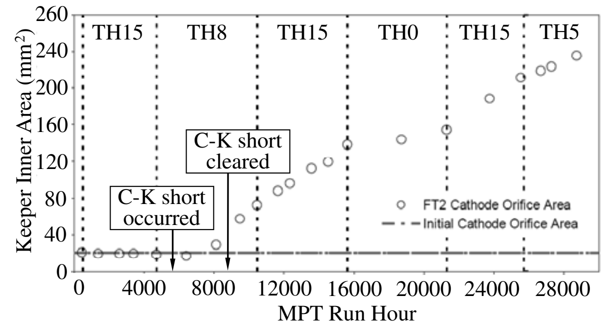

Fig. 3 Evolution of the keeper-orifice channel enlargement during the ELT showing accelerated erosion after ∼8000 h.

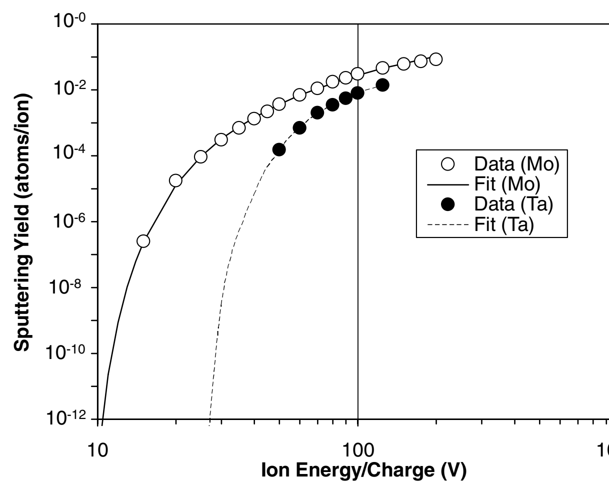

Fig. 4 Sputtering yield for Mo and Ta as a function of Xe ion energy. The experimental uncertainty for the low-energy values (<60 V) is ±20–30% for Mo and approximately ±40% for Ta.

III. Theoretical Model

The two-dimensional computational model solves the conservation laws for three species present in the partially ionized gas: electrons, xenon ions, and xenon neutrals. It is assumed that only singly charged ions are present and that the ionized species satisfy quasi neutrality $n \equiv n_e = n_i$. The computational region employed for the DHC simulations is illustrated in Fig. 5. It spans the cathode interior, cathode and keeper orifices, and the cathode's near-plume and far-plume/anode regions. The gap between the keeper and cathode plates is not modeled; the imposed boundary conditions assume that the plate wall covers the gap. The computational grid consists mostly of rectangular cells inside the cathode but transitions to a generalized grid arrangement in the plume region. The plume grid is constructed by first aligning as close as possible grid lines along the magnetic field streamlines. Then the perpendicular grid lines are generated in a way that preserves orthogonal computational cells as much as possible. This is achieved better in regions of high magnetic field strength compared with regions of low field strength. An algorithm that generates an "exact" magnetic field mesh (using streamlines and stream functions) has not been incorporated in the present simulations. The applied magnetic field is shown in Fig. 6. At the keeper-orifice exit, the field strength is approximately 90 G, in close agreement with the strength of the field in this region during thruster operation.

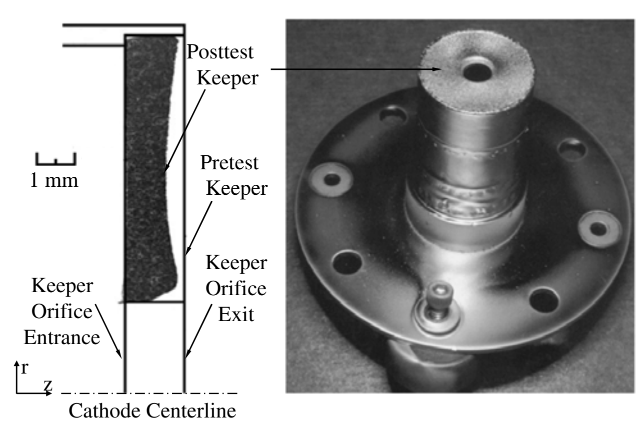

Fig. 1 The DHC keeper after the 8200 h LDT of a 30-cm ion thruster. Left: cut-away view of the keeper plate. Right: the cathode assembly showing the eroded keeper plate.

A. Conservation Laws and Boundary Conditions

The conservation laws in the absence of an applied magnetic field as well as the boundary conditions have been described in a companion paper [17]. Thus, only those equations that have been augmented with the appropriate terms due to the presence of the magnetic field are presented here. Boundary conditions that are associated with the extended plume/anode region and the approach to account for anomalous transport of electrons are also discussed.

Equation (1) expresses the inertia-less electron momentum equation in Ohm's-law form and includes the electron Hall-effect

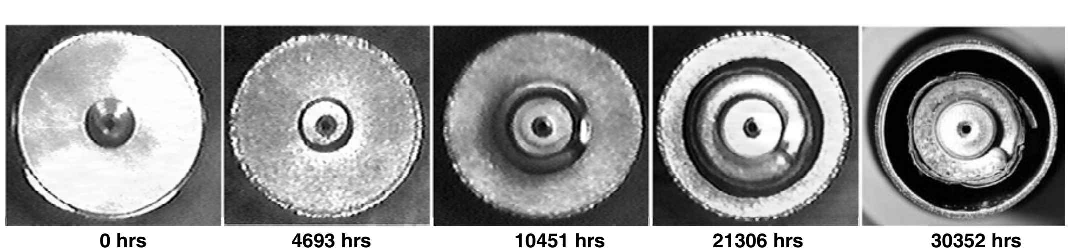

Fig. 2 Front view of the DHC keeper at various times during the 30,000 h ELT of a 30-cm ion thruster.

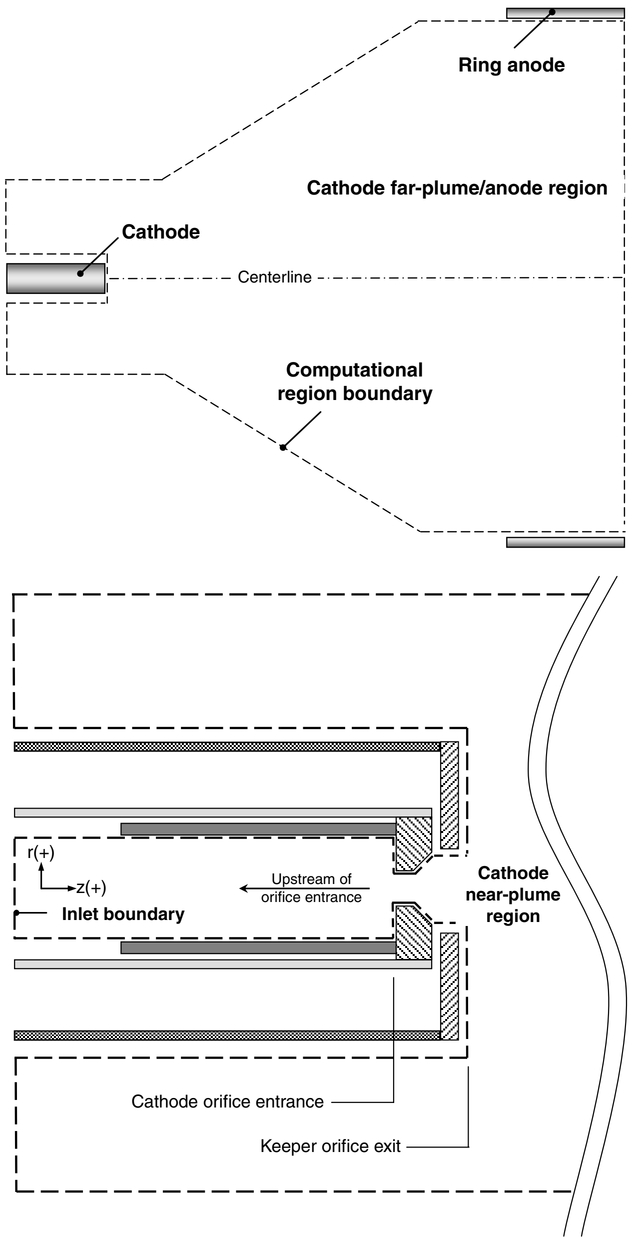

Fig. 5 Schematic of the DHC outlining (by the dashed line) the computational region employed in the numerical simulations. Top: far-plume/anode region. Bottom: cathode interior and near-plume regions. The "near plume" is defined as the region of plasma within a radius of a few centimeters downstream of the keeper-orifice exit.

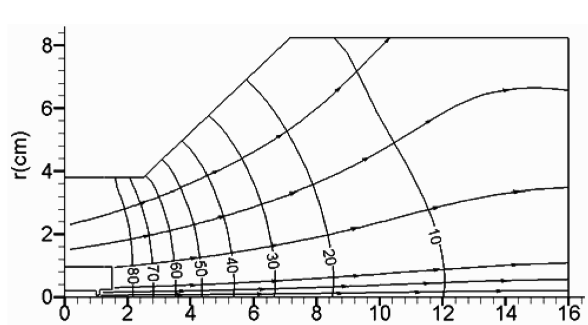

Fig. 6 Applied magnetic field used in the hollow cathode simulations. Shown are magnetic field streamlines overlaid by axial-component (B_z) contours in gauss.

term. The ion current term in Eq. (1) is a direct product of the friction force on the electrons, which, in the case of small electron drifts, is linearly dependent on the relative velocity between electrons and ions and on the (classical) electron-ion ($e-i$) collision frequency: $\nu_{\mathrm{ei}}(\mathbf{u}_e-\mathbf{u}_i)$. If plasma turbulence is present, the friction on the electrons can be enhanced, and the effect is many times accounted for by adding an "anomalous" collision frequency ν_a to the classical value [Eq. (2)]. These are idealized approximations that must be reevaluated in cases of strong microturbulence in which significant distortions of the electron energy distribution function (EEDF) can occur in the bulk electrons.

$$\mathbf{E}'\equiv\mathbf{E}+\frac{\nabla p_e}{en}=\eta\mathbf{j}_e+\frac{\mathbf{j}_e\times\mathbf{B}}{en}+\frac{m_e\tilde{\nu}_{\mathrm{ei}}}{e^2n}\mathbf{j}_i \tag{1}$$

$$\eta=\frac{m_e\nu_{\mathrm{en}}}{e^2n}+\frac{m_e\tilde{\nu}_{\mathrm{ei}}}{e^2n},\qquad \tilde{\nu}_{\mathrm{ei}}\equiv\nu_{\mathrm{ei}}+\nu_a \tag{2}$$

In the computational model, the governing laws that include the applied magnetic field are first solved in the frame of reference of the magnetic field. For example, the electron current density components parallel and perpendicular to the magnetic field are given by

$$j_{e,\|}=\frac{E'_{\|}-\tilde{\eta}_{\mathrm{ei}}j_{i,\|}}{\eta}\qquad j_{e,\perp}=\frac{E'_{\perp}-\tilde{\eta}_{\mathrm{ei}}j_{i,\perp}}{\eta(1+\Omega_e^2)} \tag{3}$$

where $\Omega_e=|\mathbf{B}|/en\eta$. The components in r-z space are then obtained by appropriate vector operations. The anisotropy of the classical e-i collision time has been evaluated by sensitivity simulations that have incorporated Braginskii's transport coefficients for the resistivity tensor in a fully ionized plasma [22]. The simulations showed differences with a maximum factor of 2 compared with the isotropic results. In light of the dominance of the anomalous resistivity in the near plume, this effect is not significant. Thus, all simulations presented herein that are associated with classical collisions assume a scalar resistivity.

The ion current density is obtained from the sum of the (inertia-less) electron and ion momentum equations as given by Eq. (4). It is noted that the ions are not magnetized in this problem.

$$\mathbf{j}_i=en\mathbf{u}_n+\frac{m_e\nu_{\mathrm{en}}\mathbf{j}_e+e\mathbf{j}_e\times\mathbf{B}-e\nabla(p_e+p_i)}{m_i\nu_{\mathrm{in}}} \tag{4}$$

The plasma potential is obtained from the current conservation law

$$\nabla\cdot(\mathbf{j}_e+\mathbf{j}_i)=0 \tag{5}$$

in combination with Eqs. (1) and (4). Both in the cathode experiments referred to herein and during thruster operation, the magnetic field is applied by ring or coil magnets, and is not varied in time. In the keeper region, the applied magnetic field is much larger than any induced magnetic field (ratio of induced over applied field is $\sim$0.1 or smaller). Therefore, it is assumed that the electric field is curl free so that $\mathbf{E}=-\nabla\phi$. Equation (5) is solved using a strongly implicit algorithm. The solution is obtained by a preconditioned, least-squares, conjugate-gradient method. The conservation equations listed previously are part of a larger system that consists of the ion and neutral continuity equations, the electron and heavy-species energy equations, and the neutral momentum Eq. (17).

The boundary conditions inside the cathode include electron emission from the emitter and have been described in detail in previous papers [15,16]. Along the keeper, boundary conditions are specified according to the same thin-sheath relationships that are prescribed inside the cathode. Namely, ions enter the sheath in accordance to the Bohm condition. Thus, the ion flux to the boundary is given by

$$(n\mathbf{u}_i)\cdot\hat{\mathbf{n}}=n_p\exp(-1/2)\sqrt{k_BT_p/M} \tag{6}$$

where the plasma density and electron temperature at the grid cell center adjacent to the wall boundary are denoted by n_p and T_p, respectively. The Bohm ion flux condition is specified at all other boundaries external to the cathode including the far-plume (outflow) boundaries and the anode.

The sheath condition for electrons along the keeper boundaries is specified by

$$\mathbf{j}_e \cdot \hat{\mathbf{n}} = -j_{e,\mathrm{th}} \exp\lfloor -e(\phi_p - V_K)/k_B T_e \rfloor \tag{7}$$

where $\phi_p - V_K$ is the voltage drop across the sheath. The plasma potential at the grid cell center located adjacent to the wall boundary is denoted by ϕ_p, and the keeper voltage is given by V_K. Collection of electrons at boundaries other than the cathode and keeper occurs only at the anode where the current density is assumed to be uniform. The choice of imposing a short ring anode as shown in Fig. 5 was based on several sensitivity simulations aimed at identifying the anode arrangement that best emulates collection at the cusps of the ring magnets inside the discharge chamber. This approach was necessary because the available computational resources do not yet allow us to encompass the full discharge chamber as part of the global computational region, which (as shown in Fig. 5) includes the cathode interior. One set of sensitivity simulations compared the anode ring arrangement as shown in Fig. 5 (bottom) with a flat-disk anode placed at the far end of the computational region ($z = 16$ cm). The results showed that the near-plume region is insensitive to such changes in the anode boundary condition.

B. Nonclassical Transport in the Discharge Plasma

Previous theoretical and experimental work with electric propulsion cathodes showed evidence of nonclassical transport in the plasma, possibly as a result of IAT. In early work with high-current (up to 60 A) hollow cathodes and an applied magnetic field, Friedly and Wilbur [23] observed plasma "noise" in the discharge and considered the ion acoustic instability as the cause of this noise after considering the experimental findings of Guyot and Hollenstein [24] with current-carrying plasmas. Based only on Langmuir probe signals, however, Friedly and Wilbur concluded that the fluctuation level was too small ($\delta\phi <$ few volts) to explain the high-energy "ion jets" observed in that cathode. More recently, Mikellides et al. [15] showed by numerical simulation of the plasma inside a DHC operating at $I_d = 25$ A (applied $\mathbf{B} = 0$) that the electron Mach number $|\mathbf{u}_e|/u_{T,e}$, electron temperature, and electron-to-ion temperature ratio were high enough to support the presence of IAT. Typical results for the 25 A cathode with classical resistivity and no applied magnetic field are shown in Fig. 7. In a later paper [14], it was shown that neither the time-averaged plasma measurements obtained by Goebel et al. [9,12] nor the numerical simulation results obtained by Mikellides et al. could be reconciled by classical Ohm's law. That is, when the time-averaged data were used directly to quantify each term in Ohm's law, the law could not be satisfied with classical resistivity alone. Equivalently, the numerical simulations [which incorporated Eq. (1) as part of the set of conservation laws] could not reproduce the time-averaged measurements using only classical resistivity. The (enhanced) value of the resistivity needed to explain the time-averaged measurements was estimated to be between 3 and 100 times the classical value.

It is found that the same conclusions regarding classical Ohm's law are applicable to the DHC studied here, which operates with an applied $|\mathbf{B}|_{\max} \sim 90$ G. The computed plasma potential for a value of $\nu_{ei} + \nu_a$ that is 1 order of magnitude less than the value ultimately used in this paper is compared against the measurement in Fig. 8. The comparison with the measurement suggests the need for a higher resistive contribution ($\eta j_{e,z}$) to the electric field as determined directly by Ohm's law. A steady-state solution could not be obtained with classical resistivity alone. Moreover, in addition to conventional Langmuir probes, Goebel et al. used emissive probes to characterize the plasma in the cathode discharge [9]. The emissive probes detected high-amplitude oscillations of the plasma potential in the near-plume region of both the 25 A cathode and in the present cathode, peaking in some cases to values that exceeded 50 V (20 V $> \delta\phi >$ 5 V). The range of observed frequencies was approximately 50–1000 kHz with 1000 kHz being the probe limit. The wave amplitudes were observed to decrease with increasing wave frequency. At the probe limit, the amplitudes were the smallest ($\delta\phi >$ 5 V).

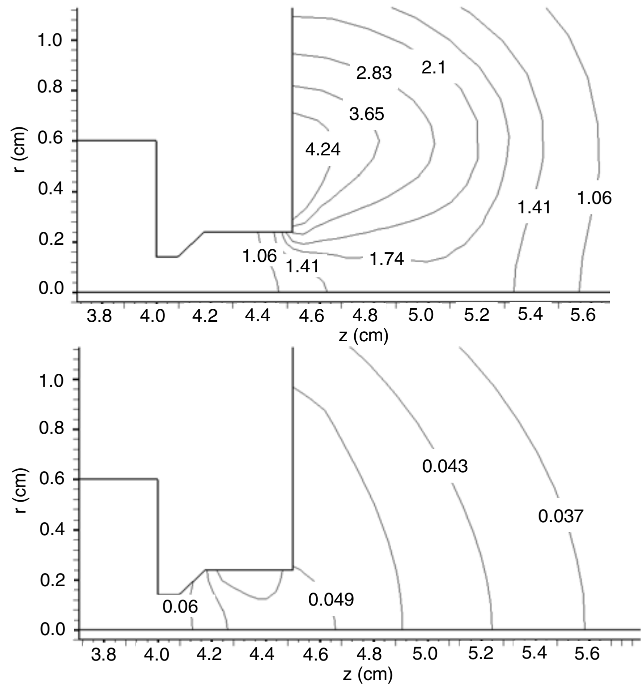

Fig. 7 Results from two-dimensional numerical simulations of a 1.5-cm, 25-A DHC operated without an applied magnetic field. The simulations assumed classical resistivity. Top: electron Mach number, $|\mathbf{u}_e|/u_{T,e}$ (from Mikellides et al. [14]). Bottom: ion-to-electron temperature ratio (T_i/T_e).

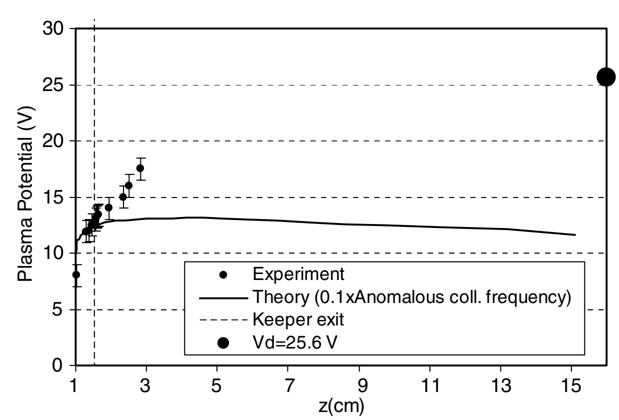

Fig. 8 Computed plasma potential along the cathode centerline for one-tenth the anomalous collision frequency used in this article. The comparison with the measurement suggests the need for additional resistivity in Ohm's law.

Ion acoustic turbulence in current-carrying plasmas has been studied extensively since the early 1960s. In a 1987 review paper on the topic, Bychenkov et al. [25] provide over 200 references related to theoretical and empirical investigations of IAT. Perhaps the most well-known early work on IAT theory was performed by Sagdeev and Galeev [26] in the late 1960s. The work produced a simple formula for the anomalous resistivity that was based on a quasi-linear interaction between particles and waves, along the lines of Kadomtsev's original work on weak-turbulence theory [27].

In the long-wavelength limit ($k\lambda_D \ll 1$) the physical picture of a current-carrying plasma with IAT is that, first, a fraction of the electrons will be accelerated by the applied electric field in the classical runaway process. Second, those electrons whose relative drift velocity u_d exceeds the ion acoustic speed $C_s = [2k_B(T_e +$

$T_i)/M]^{1/2}$ will participate in a quasi-linear interaction with the ion sound waves, and this latter interaction will lead to an enhancement of the resistivity relative to the classical value. Sagdeev proposes that in a plasma with IAT, the analogy with the classical runaway process in a Lorentz gas is simply that the retarding classical collisions are now the "collisions" of electrons with the electrostatic waves [26]. The analogy is based on the quasi-linear wave collision term as derived by Sagdeev that has the same power dependence on velocity as the classical collision integral in a Lorentz gas (inverse fifth power). Electrons not resonant with the ion sound waves run away. The fraction of runaway electrons depends in part on the strength of the electric field. The time-averaged measurements along the centerline of the DHC suggest that, in some regions of the near plume, the local electric field exceeds the classical Dreicer [28] critical value E_c for runaway electrons in a fully ionized plasma

$$E_c = 0.43 E_D, \qquad E_D = \frac{e^2 \ell n \Lambda}{4\pi\varepsilon_0^2} \frac{n}{k_B T_e} \tag{8}$$

as shown in Fig. 9. Because the electric field in these regions is seen not to exceed greatly the critical value E_c, it is hypothesized that the fraction of electrons that run away parallel to the magnetic field is relatively small, and that the bulk electrons interact quasi linearly with the ion sound waves. It should be noted that even if the fraction of runaway electrons is small, they may still carry a large fraction of the current due to their high drift velocities. These "high-energy" electrons also lead to greater ionization in the discharge chamber compared with the thermalized population.

Several investigators have attempted to derive idealized mathematical models of the effective resistivity in plasmas with IAT. The results have varied, in some cases by orders of magnitude. Herein, we refer to only a few of these models but point the reader to Bychenkov et al.'s review paper [25], in which several other such attempts are referenced. In its most general form, the anomalous collision frequency for IAT may be expressed as

$$\nu_a \approx \omega_{pe} \frac{W}{n k_B T_e} \tag{9}$$

where W represents the total energy density associated with the turbulent-wave fluctuations:

$$W = \frac{\varepsilon_o}{2} \langle s(\omega_k, \mathbf{k}) |\delta \mathbf{E}(\mathbf{k})|^2 \rangle \tag{10}$$

In Eq. (10), $\delta\mathbf{E}(\mathbf{k})$ is the turbulent electric field fluctuation and $s(\omega_k, \mathbf{k})$ is the nonlinear plasma response function. The angular brackets indicate averaging over the whole spectrum of fluctuations. Much of the physical and mathematical complexity of determining the anomalous collision frequency is associated with identifying this energy spectrum. Sagdeev's mathematical model produced a linear dependence of the anomalous collision frequency on the electron-to-ion temperature ratio, the ion plasma frequency and u_d/C_s as follows: $\nu_a \sim \omega_{\mathrm{pi}}(T_e/T_i)(u_d/C_s)\ \mathrm{s}^{-1}$, which can be orders of magnitude greater than the linear growth rate. Later, a multiplication factor of 10^{-2} was implemented that made the expression an approximate equality [29]. Despite the factor 10^{-2}, it is found that in the DHC studied here, Sagdeev's collision frequency overestimates the value needed to explain the measurements by more than 2 orders of magnitude in the near plume.

Based largely on the DHC time-averaged measurements [13] of the plasma density and electron temperature, a typical value of the ratio u_d/C_s at the keeper-orifice exit is found to be approximately 140. In plasmas with high enough electric fields such that $u_d/C_s \gg 1$, Galeev provides an asymptotic value of the collision frequency [30]:

$$\nu_a \sim [M/m_e]^{1/2} \omega_{\mathrm{pi}} C_s / u_d \ \mathrm{s}^{-1}$$

In the high-field limit, Bychenkov [25] also provides an expression for the resistivity in terms of the electric field (from Zavoiskii and Rudakov [31]), which can be used to obtain the anomalous collision frequency as follows:

$$\nu_a \approx 813.5 E^{1/2} [n/k_B T_e]^{1/4} \ \mathrm{s}^{-1}$$

In the plume region of the DHC, Sagdeev, Galeev, and Bychenkov's models are compared with the present model as well as with the classical electron collision frequencies along the centerline in Fig. 10. The classical e-i collision frequency $\nu_{\mathrm{ei}} \sim n/T_e^{3/2}$, as determined using the measured density and electron temperature, is also plotted in Fig. 10. The main reason for including this "measured" frequency ν_{ei} in Fig. 10 is to show that the experiment also predicts classical e-i collision frequencies that are too low compared with the values needed to account for the measured plasma

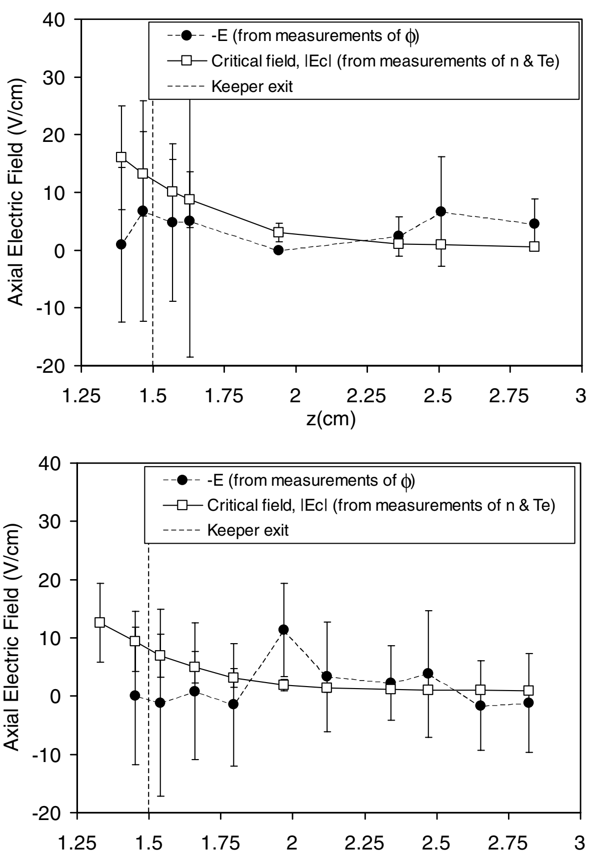

Fig. 9 Electric field derived directly from the time-averaged plasma potential measurements compared with the Dreicer critical electric field derived from the plasma density and electron temperature measurements. Top: TH15. Bottom: TH8.

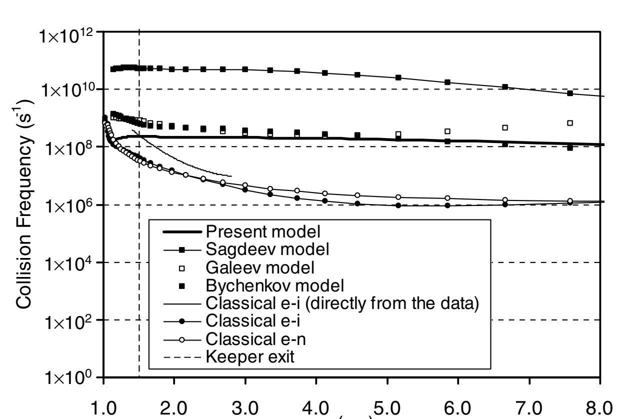

Fig. 10 Comparison of characteristic frequencies along the cathode centerline. Unless otherwise indicated, all values in the figure are determined based on the numerical simulation results for the plasma parameters at TH15.

potential and electron temperature in the near plume. This observation was found to be true in previous work also [14] performed by the authors for a different cathode in which anomalous resistivity was invoked based on existing theoretical models. In the present work, the plasma model for the anomalous collision frequency has been based largely on the time-averaged measurements. Attempts to produce a theoretical model of the DHC turbulence have not yet been undertaken. Sensitivity simulations indicate that the results are not sensitive to small spatial variations of the effective collision frequency. In fact, it is found that a fixed value of $\nu_a = 2 \times 10^8\ \mathrm{s}^{-1}$ everywhere in the plume produces minimal changes in the time-averaged results.

The comparison of the various frequencies in Fig. 10 suggests that damping of the waves is likely taking place inside the keeper orifice because the classical collision frequency is observed to increase rapidly with distance upstream of the keeper exit and ultimately prevails over the anomalous frequency (solid curve). Landau damping of ion acoustic waves would occur in this region due to an increase in the ion temperature relative to the electron temperature. Collisional damping of the waves can also occur as a result of increased collisions of ions with neutrals and/or due to the increased loss rate of ions into the orifice channel sheath. Once inside the channel, Fig. 11 shows that the computed ion-neutral collision frequency becomes a substantial fraction of the measured wave frequencies in the near plume and ultimately exceeds them near the entrance to the keeper orifice. Later, it will be shown that the keeper erosion predictions well inside the orifice channel require lower-amplitude waves compared with those observed outside the channel, which supports the hypothesis of reduced turbulence inside the keeper orifice.

In regards to the early (1960s–1970s) theoretical predictions of the anomalous collision frequency in a plasma with IAT, it should be noted that later advancements in computation allowed for a more extensive investigation of the saturation mechanisms. Numerical simulations to quantify the anomalous resistivity in IAT have used a variety of particle-based methods, most commonly particle-in-cell (PIC). As with the analytical results, the numerical results have also varied, in some cases by orders of magnitude. In a comprehensive review of past computational attempts on the subject, Büchner and Elkina [32] state that PIC-code simulations have not yet been able to establish a general expression for the anomalous resistivity because no stationary state of the ion sound turbulence could be established.

Despite the apparently large quantitative disparity in analytical and numerical models of IAT-driven anomalous resistivity, the five-decades-long body of work in this area points clearly to the following distinctive phenomenological features of current-carrying IAT: the saturation of the electron drift, the anomalous heating of electrons and ions, and the presence of runaway electrons. Our recent theoretical and experimental work with ion propulsion cathode discharges suggests the presence of all of these mechanisms in the near-plume plasma.

A final note on the subject is that most of the IAT theoretical models mentioned previously make several simplifying assumptions, such as no collisions with other particles (or surfaces) and homogeneous plasma in one dimension parallel to (or in the absence of) an applied magnetic field. Of particular importance are the assumptions on homogeneity because a new class of plasma instabilities may be generated in the presence of density and/or magnetic field gradients. As it will also be shown later in comparisons of the simulation results with the measurements, it is found that the steady-state plasma expansion downstream of the keeper is associated with density gradients that are comparable to the local electric field. To better illustrate this, the various force terms in the electron momentum equation are compared along the axis of symmetry in Fig. 12. Specifically, the electron momentum equation in the z direction (parallel to $\mathbf{B}$) is given by

$$0 = \frac{R_e}{en} + \left(\underset{(I)}{\frac{d\phi}{dz}} - \underset{(II)}{\frac{1}{en}\frac{dp_e}{dz}}\right) \tag{11}$$

R_e represents the friction force on the electrons that for small electron drifts relative to the thermal velocity would depend linearly on the relative velocity; for example, for e-i collisions, $R_e = R_{\mathrm{ei}} = -nm_e\nu_{\mathrm{ei}}(u_{e,z} - u_{i,z})$. The force terms in the parenthesis of Eq. (11) are determined using the time-averaged measurements of the plasma potential, density, and electron temperature along the cathode centerline. The comparison shows the significance of the pressure-gradient force on the expansion of the electron flow from the keeper orifice. Nonhomogeneities in the density and/or applied magnetic field can lead to a wide range of "drift" instabilities in the discharge plasma.

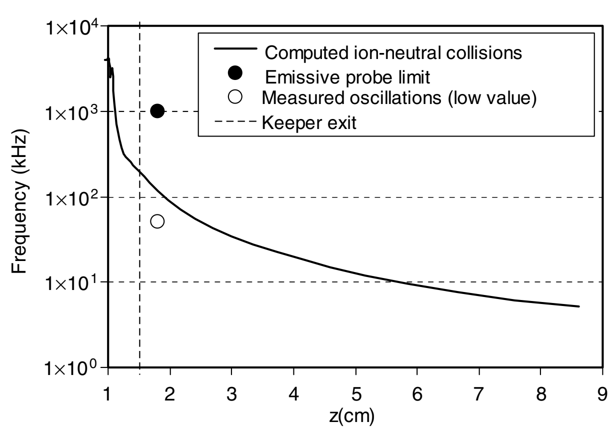

Fig. 11 Computed ion-neutral collision frequency along the axis of symmetry compared with the range of wave frequencies measured in the near-plume of the cathode. The comparison suggests that increased collisional damping would occur to ion acoustic waves inside the keeper-orifice channel. Note: the wave amplitudes were observed to decrease with increasing frequency.

IV. Numerical Simulation Results

A. Plasma Simulations and Comparisons with Measurements

Thus far, energy conservation for ions and neutrals has assumed that the heavy species are in thermal equilibrium at temperature T_h, an assumption that was largely based on the short thermal-equilibration times that occur *inside* the cathode. Thus, in the model, only a single energy equation is currently solved for the heavy species. However, in a plasma with IAT, ions may be heated as a result of scattering with ion sound waves, and this heating has been observed or theorized under a variety of plasma conditions (e.g., see [31,33–36]). In addition to the IAT-related work ion heating has also been reported in cathodes similar to the one studied here [37].

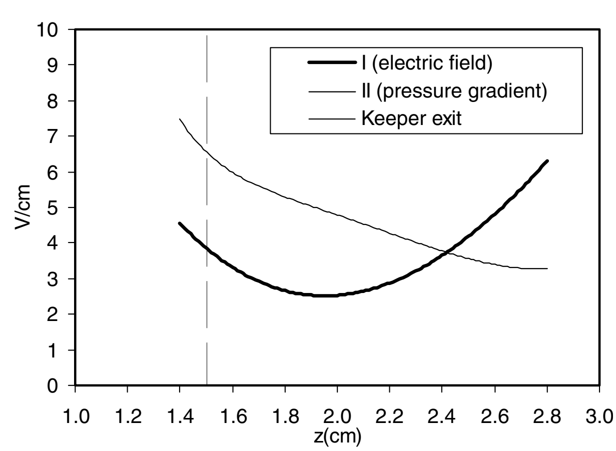

Fig. 12 Comparison of forces (per unit charge) in the electron momentum equation computed directly from the measurements: electric field versus pressure gradient along the cathode centerline.

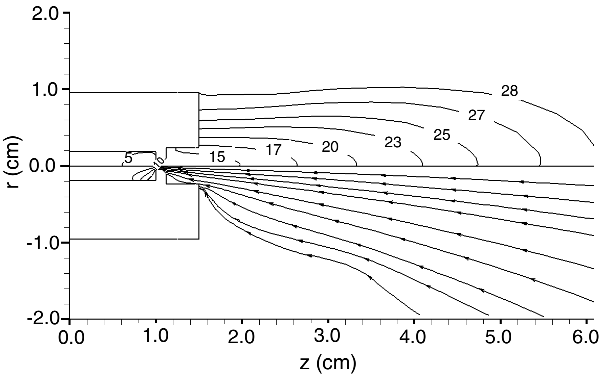

Fig. 13 Cathode near-plume solution from the numerical simulations at TH15 for the idealized case $T_e = T_i$. Top half: plasma potential (in volts). Bottom half: electron current density ($\mathbf{j}_e = -en\mathbf{u}_e$) streamlines (note: the velocity flow field of electrons and the $\mathbf{j}_e$ streamlines are in opposite directions).

When the ions are in thermal nonequilibrium with the electrons and the neutrals, then this would be modeled, ideally, by separating the single heavy-species energy conservation law into ion and neutral energy equations if the heating were due to classical collisions. The anomalous heating of ions, however, is not straightforward because the redistribution of the ion energy in IAT may also lead to changes in the equilibrium ion distribution function. In this paper, results for two limiting cases are presented: $T_e \neq T_i = T_h$ (the original assumption) and $T_e = T_i$. In light of the purely classical behavior of the plasma inside the cathode, the condition $T_e = T_i$ is applied only downstream of the keeper-orifice entrance where both the calculations and the measurements suggest that wave motion has a significant impact on

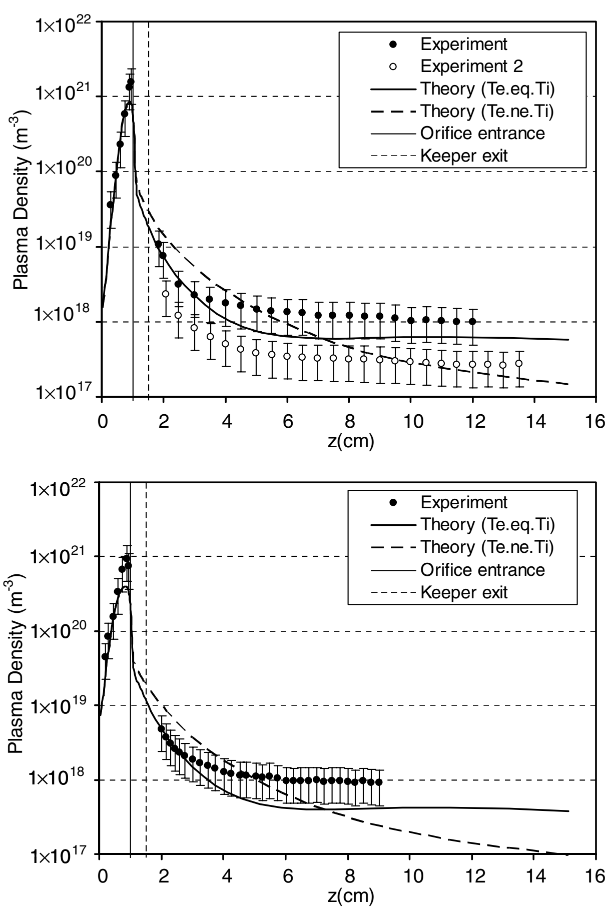

Fig. 14 Comparison between numerical simulation results and measurements: plasma density along the cathode centerline at TH15 (top) and TH8 (bottom).

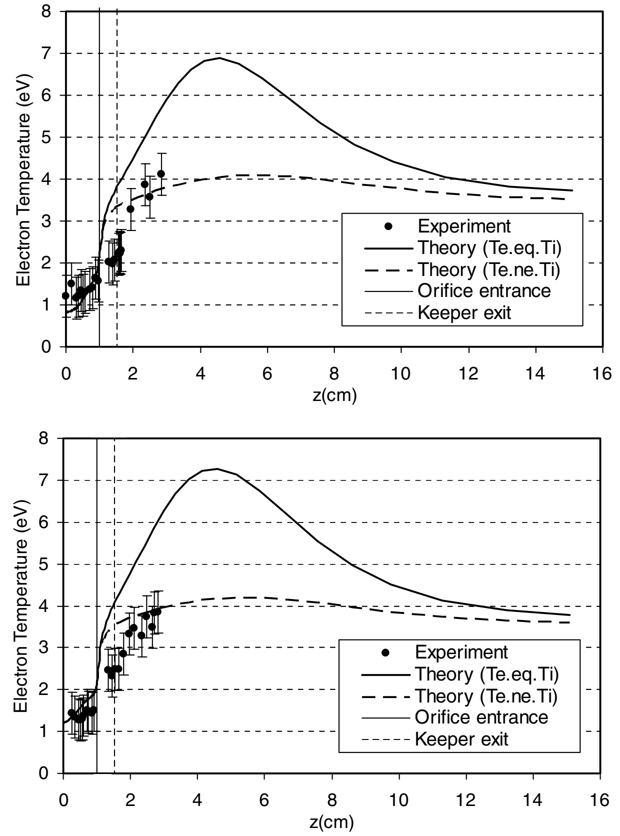

Fig. 15 Comparison between numerical simulation results and measurements: electron temperature along the cathode centerline at TH15 (top) and TH8 (bottom).

the plasma properties. Typical results are shown in Figs. 13–18. It is noted that the condition $T_e = T_i$ is implemented only in the pressure-gradient terms of the ion momentum equation because this is where the assumption impacts the results the most. That is, for the case $T_e = T_i$, Eq. (4) is altered from the original form

$$\mathbf{j}_i = en\mathbf{u}_n + \frac{m_e \nu_{\text{en}} \mathbf{j}_e + e\mathbf{j}_e \times \mathbf{B}}{m_i \nu_{\text{in}}} - \frac{e}{m_i \nu_{\text{in}}} \nabla n k_B (T_e + T_h) \qquad T_e \neq T_i = T_h \tag{12}$$

to

$$\mathbf{j}_i = en\mathbf{u}_n + \frac{m_e \nu_{\text{en}} \mathbf{j}_e + e\mathbf{j}_e \times \mathbf{B}}{m_i \nu_{\text{in}}} - \frac{e}{m_i \nu_{\text{in}}} 2\nabla (n k_B T_e) \qquad T_e = T_i \neq T_h \tag{13}$$

The implementation of the condition is, therefore, intended to provide only a preliminary assessment of the impact of ion heating on the plasma. A self-consistent assessment of ion heating would require in part a (third) energy equation for the ions as well as a reassessment of the anomalous resistivity because an increase in the ion temperature for a given electron temperature also increases Landau damping of the ion waves. It is well known that the ideal ion acoustic instability in an unmagnetized, collisionless plasma occurs when $T_e \gg T_i$.

Based on the numerical simulations perhaps the strongest evidence in support of ion heating is illustrated in Fig. 18, which plots the plasma potential as a function of radius, 3 mm downstream of the keeper-orifice exit. The comparison of the results with the plasma potential measurement shows clearly that for "cold" ions, the predicted values are in both qualitative and quantitative disagreement with the measurement. The measurements were obtained by Goebel et al. using emissive probes and have been described in a previous paper [9]. The radial plasma density shown in Fig. 17 also

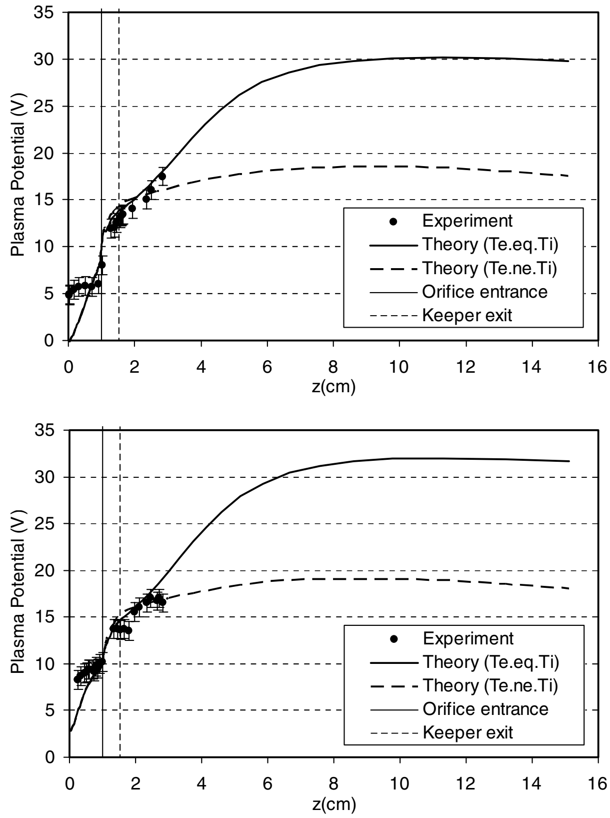

Fig. 16 Comparison between numerical simulation results and measurements: plasma potential along the cathode centerline at TH15 (top) and TH8 (bottom).

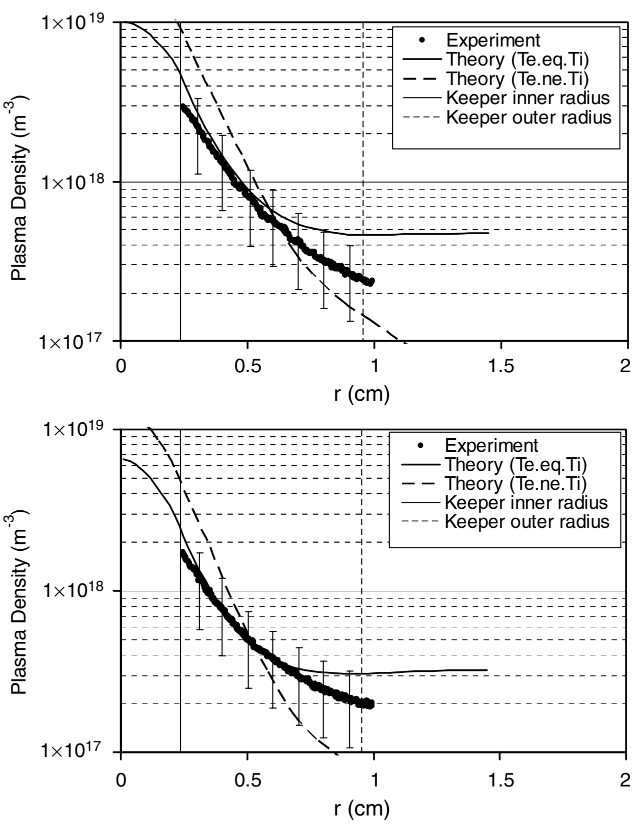

Fig. 17 Comparison between numerical simulation results and measurements: plasma density as a function of radius, 3 mm downstream of the keeper-orifice exit at TH15 (top) and TH8 (bottom).

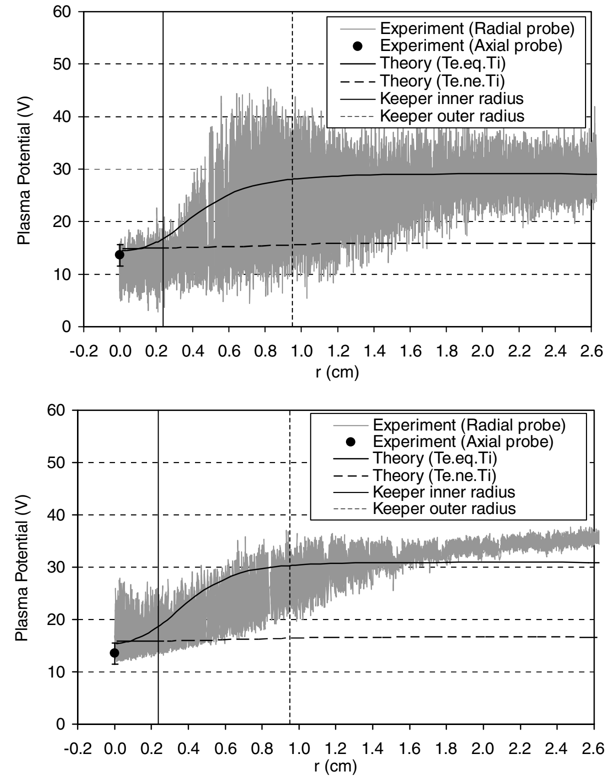

Fig. 18 Comparison between numerical simulation results and measurements: plasma potential as a function of radius, 3 mm downstream of the keeper-orifice exit at TH15 (top) and TH8 (bottom).

supports the presence of ion heating. Both radial comparisons further suggest that ions cool as they expand radially across the magnetic field lines.

Comparisons with the data along the cathode centerline are shown in Figs. 14–16. The largest discrepancies in the numerical simulation results between the two temperature cases ($T_e \neq T_i$ and $T_e = T_i$) are most evident in the electron temperature (Fig. 15) and plasma potential (Fig. 16), and occur 1–6 cm downstream of the keeper exit. As a result of the anomalous resistivity, the fluid-electron model predicts enhanced heating of the electrons in this region with temperature in the range 7.25 eV $> k_B T_e >$ 4 eV. The true value of the electron temperature in this region depends in part on the extent of the ion heating but also on the EEDF. It is observed that the Langmuir probe traces in this region exhibit extended "knees" in the electron saturation region from which a single value of the electron temperature or plasma potential is indistinct. It was also shown previously (Fig. 9) that electrons in this region can exceed the Dreicer field and run away. The observations suggest that the near-plume region is rich with wave motion that can lead to nonclassical transport of electrons and possibly of ions. While recognizing the fundamental limitations of an electron/ion-fluid model, the two simulation cases provide us with a bound on the plasma parameters in the keeper region based on which we proceed to address the erosion of the keeper. Finally, it is noted that, for a given operating point, plasma measurements have commonly shown variations in the plasma conditions established in the cathode. This is many times due to the conditioning of the emitter. As an example, Fig. 14 (top) compares the plasma density in the cathode plume measured in two different experiments of the same cathode, for the same operating condition in the same vacuum chamber. The time elapsed between these two experiments was more than 1 year.

B. Keeper Erosion Results and Comparisons with Observed Profiles

1. Life Demonstration Test (8200 h)

Because the keeper was completely eroded by the end of the ELT, the LDT is the only source of data for which an erosion profile of the

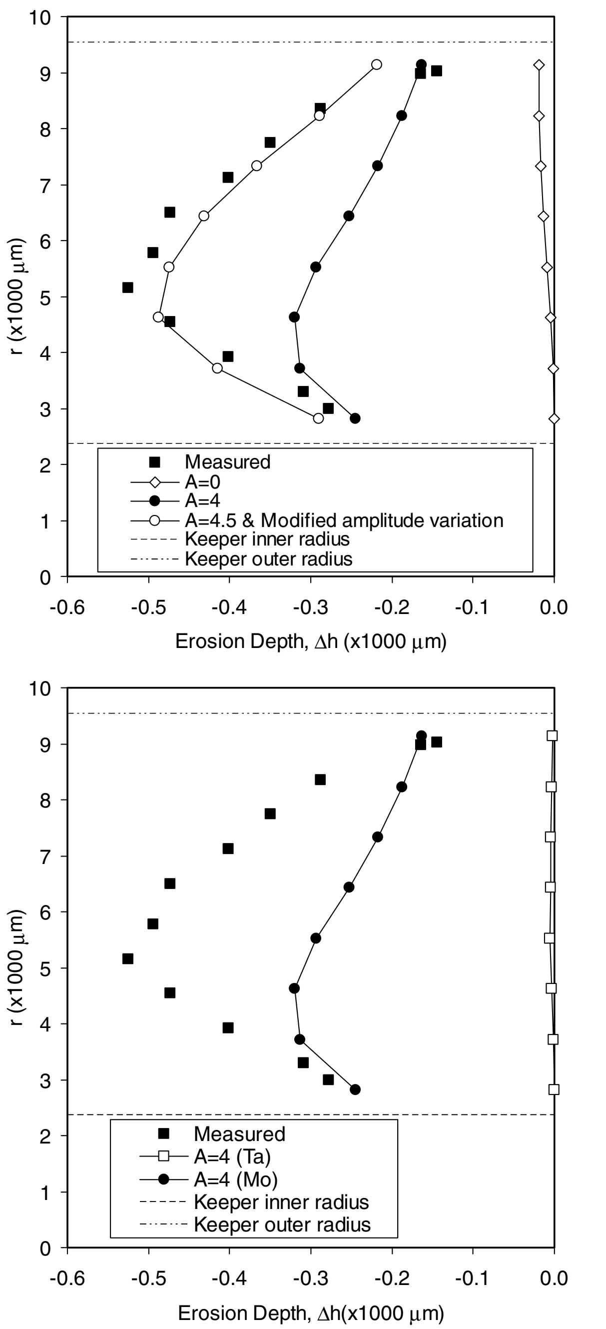

Fig. 19 Comparison between numerical simulation results and measurements: erosion of the keeper plate after the completion of the 8200 h LDT. Top: results from different models for molybdenum. Bottom: results from the same model ($A = 4$) for molybdenum versus tantalum.

keeper surface that faces the cathode plume is readily available and can, therefore, be compared directly with results from the numerical simulations. In a companion paper, it is shown that singly charged ions accelerated (classically) into the eroding surface by the sheath was sufficient to explain the erosion patterns observed in the orifice of a neutralizer hollow cathode [17]. For the keeper, it is found that this is not the case. The erosion depth (or height) Δh along the keeper face can be expressed as

$$\Delta h = (nu_{i,\perp}) Y \Delta t \frac{\mathrm{AW}}{\rho N_{\mathrm{AV}}} \tag{14}$$

Assuming that only singly charged ions with energy $\varepsilon_i = e\Delta\phi_s$ strike the surface at normal angle of incidence, Δh is plotted in Fig. 19 (diamond symbols) for $\Delta t = 8200$ h. For this calculation, the computed (nonoscillatory) values for the Bohm ion flux $nu_{i,\perp} = n\exp(-1/2)(k_B T_e/M)^{1/2}$ and sheath potential difference $\Delta\phi_s = \bar{\phi}_p - V_K$ have been used. The computed average plasma potential $\bar{\phi}_p$ along the keeper face is depicted by the (thick) solid curve in Fig. 20. The predicted erosion Δh in Fig. 19 underpredicts the observed maximum erosion by almost 2 orders of magnitude. As significant is the qualitative disagreement: the observed erosion exhibits a minimum at $r \sim 0.5$ cm, whereas the predicted erosion follows a monotonic profile as a function of radius. The results further show that the predicted time-averaged plasma potential, which largely drives the erosion predictions, varies monotonically with radius. Because of the strong dependence of the sputter yield on the ion energy (Fig. 4 or Fig. 20, bottom) the reduction of the ion flux with increasing radius is relatively benign. As a consequence, the ion flux plays no significant role on the qualitative behavior of the predicted profile.

The erosion result (in the diamond symbols) is obtained using values of the sputtering yield that depend directly on the time-averaged value of the plasma potential $\bar{\phi}_p$:

$$Y_{\mathrm{avg}} = Y(\bar{\varepsilon}), \qquad \bar{\varepsilon}_i = e(\bar{\phi}_p - V_K) \tag{15}$$

However, if the plasma potential undergoes significant oscillations as shown in Fig. 18, the effective yield can be greatly underpredicted if the time-averaged ion energy is used. To illustrate this, it is first recognized that the effect of IAT is to introduce fluctuations in the plasma potential that are in the order of a few $k_B T_e$ in amplitude. An idealized approach to emulate the oscillations is then to augment the time-averaged value with a pure sinusoid as follows:

$$\phi_p(r) = \bar{\phi}_p(r) + A(k_B T_e)\cos(\alpha r) \tag{16}$$

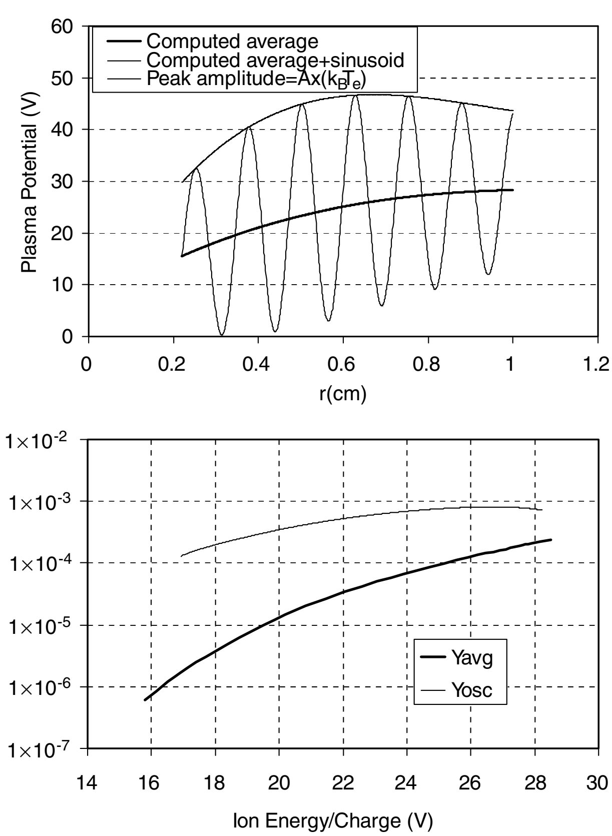

Fig. 20 Top: time-averaged plasma potential superimposed by sinusoid with peak amplitude $A \times (k_B T_e)$ ($A = 3.25$, $\alpha = 50$). Bottom: sputter yield for Mo based on the time-averaged ion energy compared with the average sputtering yield based on the ideal-oscillator model for the ion energy ($A = 3.25$, $\alpha = 500$). Note: ions are assumed to strike the surface at normal angle of incidence.

where A is the amplitude factor, and α is a value used to specify the frequency of the sinusoid. A typical sinusoid for ϕ_p is superimposed on the average value in Fig. 20 (top). In the presence of the ideal oscillator, the effective value of the yield is then determined by

$$Y_{\mathrm{osc}} = \bar{Y}(\varepsilon_i), \qquad \varepsilon_i = e(\phi_p - V_K) \tag{17}$$

The barred symbol is used to indicate that the averaging is performed on the yield, not on the ion energy. The values from Eqs. (15) and (17) are compared in Fig. 20 (bottom) for typical ion energies near the keeper. Y_{osc}, in this example, was determined by evaluating $Y(\varepsilon_i)$ at 780 radial positions and then obtaining the average value at every 78 positions. The value of α was 500 and was chosen such that the computed yield improves only negligibly in accuracy by increasing the resolution of the sampling (it is noted that α in this context has no physical significance). The comparison in Fig. 20 (bottom) shows that the effective yield can be altered significantly by the presence of the oscillations, especially at the lower values of the plasma potential, where the yield has a stronger dependence on the ion energy. This estimate does not yet take into account the fluctuations in the plasma density, which would also affect the sputtering yield.

The impact of Y_{osc} on the erosion prediction is illustrated in Fig. 19 (top, circled symbols). The comparison between the predicted and the observed profiles shows a better quantitative and qualitative agreement by contrast to the result based on Y_{avg} (diamond symbols). The choice of $A = 4$ in Fig. 19 (filled circles) was based on the maximum amplitude measured by the emissive probe, which was a little over 45 V (Fig. 18, top). The spatial variation of these amplitudes largely determines the erosion profile. Because the numerical simulation seeks only the steady-state solution, this variation can only be modeled ideally by using a constant amplitude factor A and the computed (steady-state) electron temperature. Although this is only an ideal approximation, a sensitivity calculation shows that the discrepancy between the computed and observed profiles in Fig. 19 (top, filled circles versus filled squares) is, in fact, not far from the experimental uncertainty associated with the time-averaged plasma measurements. For example, the computed profile depicted by the empty circles in Fig. 19 (top), which closely matches the observation, requires 1) a spatial variation in the wave amplitude (or more precisely in T_e because A is fixed) that is close to the experimental uncertainty associated with the electron temperature, and 2) $a \sim 13\%$ increase in A. The computed and modified electron temperature profiles used to produce the erosion profiles in Fig. 19 are compared in Fig. 21. The discrepancy between the two profiles is within $\pm 20\%$ along the keeper face.

Other physics, not accounted for by the present model, may also be contributing to the discrepancy between the $A = 4$ prediction (filled circles) and the observation (filled square symbols) in Fig. 19. The double-to-single ion current ratios in the ELT ion engine have been reported to be in the range of 0.02–0.2 [38] (but the values near the keeper are unknown), and typical values of the electron temperature near the keeper are computed here to be as high as ~6 eV. Based on these values, the suggestion then is that doubly charged ions may be playing a nonnegligible role on the erosion. Because the present model computes self-consistently all the variables associated with ionization, it is possible to determine the ratio of double and single ionization rates $\ddot{n}/\dot{n}$ near the keeper surface. If it is assumed that all ions generated near the keeper bombard the surface then this ratio would also be proportional to the double-to-single ion flux ratio. Based on our computed values, we find that, along the keeper surface, this ratio does not exceed 0.03 (see Fig. 22). This result is based on measured [39] ionization cross-section values for the $e + \mathrm{Xe}^{+} \rightarrow \mathrm{Xe}^{++}$ reaction that have been averaged over a Maxwellian distribution function. If we neglected the effective increase of the sputtering yield as a result of the wave motion, that is, if we determined the yield using Eq. (15) (also thick curve in Fig. 20), then the maximum erosion by doubly charged ions is found to be ~7 times that caused by singly charged ions, and this maximum occurs near the inner radius of the keeper ($r \sim 0.25$ cm). At this location, the erosion based on Eq. (15) is more than 3 orders of magnitude less than the observed value, and so the seven-fold increase due to Xe^{++} makes a negligible difference. If the wave motion is accounted for, and Eq. (17) is used, then we find that erosion by Xe^{++} can be as high as one-half that caused by Xe^{+}. Thus, the observed discrepancy in Fig. 19 (filled circles versus filled squares) may also be the result of neglecting Xe^{++} in the present computational model.

Despite the complexities of the wear mechanisms that are largely due to the wave motion, practical approaches to reduce substantially keeper erosion are still viable: 1) use materials with much lower sputter yield, and/or 2) raise the keeper voltage relative to the cathode by a few volts, as already proposed by Kolasinksi and Polk [40]. The benefits from the latter approach will have to be compared with losses in performance due to the increased electron collection by the keeper. Because the plasma potential is so high in the keeper region, such losses are expected to be small. In regard to alternative keeper material, an example of the predicted erosion between Mo and Ta is compared in Fig. 19 (bottom) under the same plasma conditions. Ta yields between 55 and 750 times less erosion compared with Mo due to its lower sputtering yield (Fig. 4). The use of Ta for the keeper has been proposed in the past; it is now used in the ion propulsion cathodes onboard NASA's DAWN mission [41]. Also, due to the very low sputtering yield of carbon [20], a graphite keeper is used in NASA's Evolutionary Xenon Thruster (NEXT) discharge cathode [42].

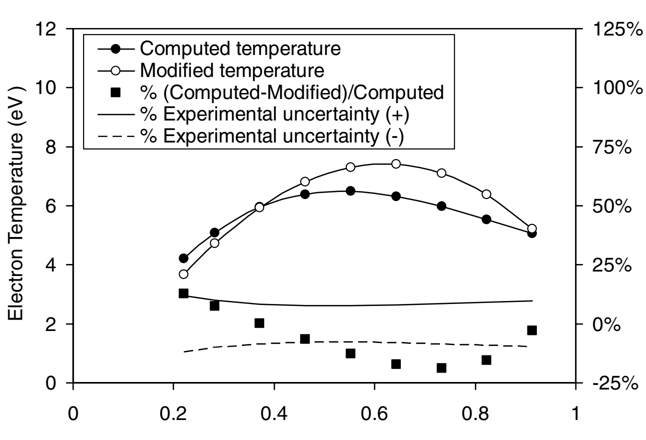

Fig. 21 Computed and modified electron temperature as a function of radius along the eroded keeper face. The precise prediction of the observed profile in Fig. 19 would require modifications in the computed amplitude that are in the order of the experimental uncertainty.

2. *Extended-Life Test*

Because the keeper plate was completely eroded in the ELT, no detailed profiles such as the one shown in Fig. 19 exist for direct comparisons with the numerical simulations. However, photographs of the keeper plate taken at various intervals during the test (Fig. 2) allow us to follow the opening of the keeper-orifice channel as a function of time. The results were first reported by Sengupta et al. [18] and are summarized in Fig. 3. Two events occurred during operation of the thruster at TH8 that are of particular interest. First, the erosion of the channel was noticed to accelerate after ~8000 h. Second, a cathode-to-keeper short occurred at $t = 5850$ h. The relation between operation at TH8 and the effect(s) of the changing plasma properties as a result of the chamfering on the accelerated erosion during/after the C–K short has never been quantified. The short was cleared at $t = 8873$ h.

In addition to the numerical simulations performed at TH15, simulations have been conducted at TH8 that incorporate the C–K short. All simulation cases are summarized in Table 3. The plasma solution is then used to determine the erosion of the channel. The predicted erosion profile after 4693 h is shown in Fig. 23 (top) for the same amplitude factor used in the keeper-face erosion calculations, namely $A = 4$, and for $A = 0$. As a result of the camera's view, the erosion profile cannot be extracted from the photograph. Thus, the results are compared with the maximum radius of the keeper channel

Table 3 Test conditions versus numerical simulation cases for the erosion calculations

Time segment, h	Extended-life test		Numerical simulation	
	Throttle level	V_K, V	Throttle level	V_K, V
0–447	TH12	4.1–4.3	TH15	4.0
447–4693	TH15	4.0–4.3	TH15	4.0
4693–5850	TH8	3.1–3.5	TH8	3.3
5850–6408	TH8	0.4 (C–K short)	TH8	0.0

as observed from the photograph. The comparison shows that, for $A = 0$ (empty circles), the erosion is too small to be detectable on the plot. For $A = 4$, the computed erosion overestimates the observed maximum ($r = 2709$ μm) by about 5%. It is noted that the 5% difference is within the uncertainty of the observed value because the latter could only be extracted from a photograph (see Fig. 23, top left corner, or Fig. 2). Assuming a fixed value of A inside the channel, the computed erosion profile overpredicts the observed erosion (also estimated from the photographs) at the entrance to the keeper channel. This implies that 1) the wave amplitudes are reduced and/or 2) redeposition of eroded material occurred. Both are likely. A reduction in the amplitude can be associated with collisional damping of the waves inside the channel. As discussed earlier, classical electron collisions as well as ion-neutral collisions (see Fig. 11) and ion loss to the walls increase significantly inside the channel. Redeposition of eroded material may have also contributed to the reduced net erosion observed near the orifice entrance, which is also evident in the LDT keeper (see Fig. 1). The quantitative resolution of both these mechanisms inside the channel, turbulence damping and material redeposition, is beyond the scope of this paper.

The predicted profile in the interval 4693–5850 h is shown in Fig. 23 (bottom). During this interval, the thruster was operated at TH8, but the C–K short had not yet occurred. The predicted profile for the time segment of 5850–6408 h, during which the C–K short was in effect, is also illustrated in Fig. 23 (bottom) by the filled-square symbols. To quantify the impact of the C–K short, the result is compared with the case without the C–K short (empty square symbols). The comparison shows that in 558 h, the C–K short contributed an additional ~50 μm to the enlargement of the channel ($r = 3.135$ mm without short versus $r = 3.184$ mm with short) and that the instantaneous erosion rate increased by 43.8%, from 0.201 mm/kh (without short) to 0.289 mm/kh (with short). Both numbers are based on the increase of the chamfered region's outer radius during this time segment but do not account for any additional enhancements due to changes in the sheath drop caused by the chamfering. Also, as already stated in Sec. III.A, the cathode-keeper gap is not accounted for in the simulations. It is assumed that the keeper plate extends to the end of the cathode plate.

To assess such changes, numerical simulations with the keeper channel chamfered to a maximum radius of ~0.3 cm were performed. The results show that the elevated plasma potential established in the near-plume region in front of the keeper plate advances upstream, toward the cathode orifice, as the channel opens (Fig. 24). For example, when the channel is chamfered, the predicted decrease of the ion flux perpendicular to the inner surface of the

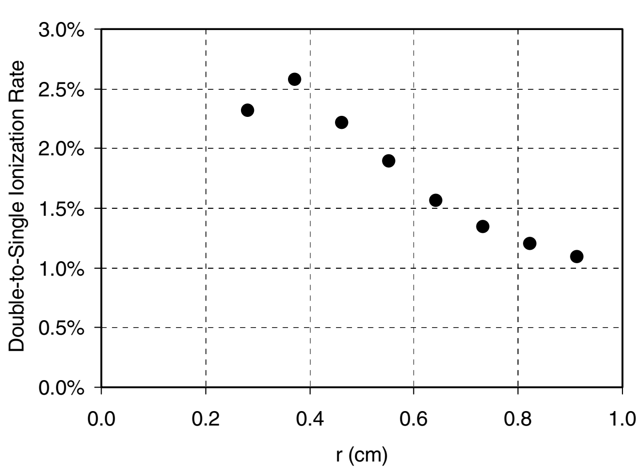

Fig. 22 Computed rate % ratio of double ($\dot{n}$) over single ($\dot{n}$) ionization as a function of radius, 0.1 mm downstream of the keeper.

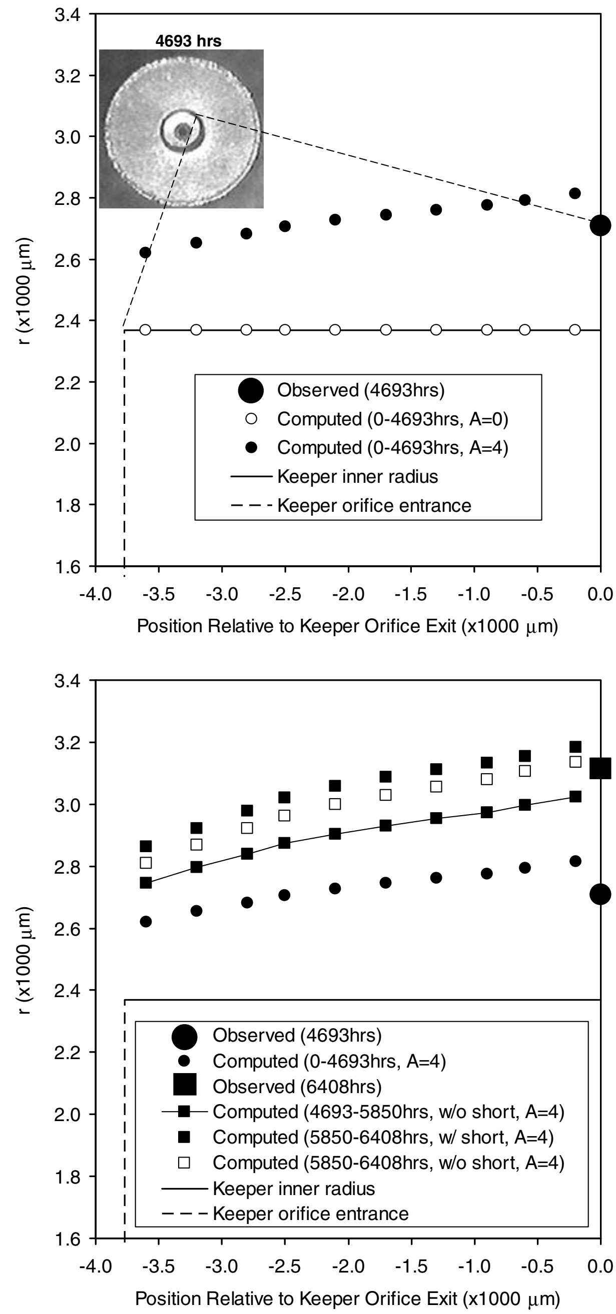

Fig. 23 Comparison between numerical simulation results and measurements: erosion of the keeper-orifice channel during the ELT. Top: 0–4693 h (TH15). Bottom: 0–6408 h (TH15 and TH8). The abscissa denotes distance (in mm) from the keeper-orifice exit in the upstream direction.

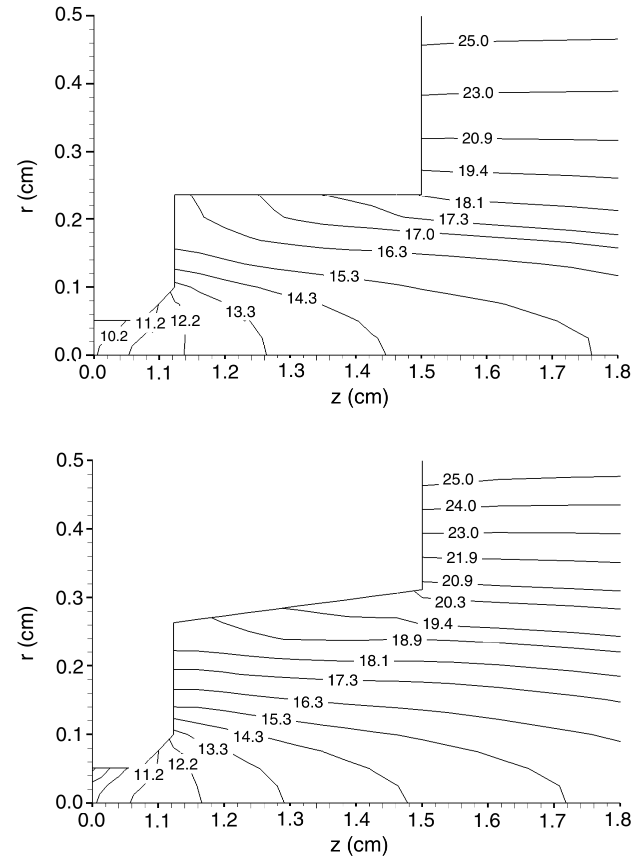

Fig. 24 Steady-state plasma potential (in volts with respect to cathode ground) in the keeper-orifice channel region from the numerical simulations at TH8. Top: without erosion of the channel. Bottom: with a chamfered channel.

keeper orifice is found to be only about 50% near the keeper exit. The ion flux decreases mainly because the ion density decreases as the keeper channel opens. Whereas the number of ions striking the surface decreases, the plasma potential (and therefore the ion energy) is found to increase from 18.1 to 20.3 V. The latter implies a 3.65 increase in the sputtering yield. Therefore, as the channel opens, the erosion accelerates. The latter value (3.65) is estimated without yet taking into account the plasma oscillations (i.e., the case is for $A = 0$). As shown in Fig. 20 (bottom), the effect of the oscillations is to raise the effective value of the yield but alleviate its strong dependence on the ion energy. For the nominal case of $A = 4$, it is found that the effective yield Y_{osc} increases by a factor of 1.78 when the ion energy/charge is increased from 18.1 to 20.3 V. By comparison to the value of Y_{avg} at the same energy, Y_{osc} is 80 times higher at 18.1 V and 39 times higher at 20.3 V. Therefore, additional acceleration of the erosion would occur if the higher amplitude oscillations in the near plume propagated into the channel.

Based on all the results presented herein, it is concluded that the observed acceleration of the keeper channel erosion was enhanced by the C–K short. It is most likely, however, that this acceleration would have occurred regardless of the short because the plasma potential, and possibly the oscillations, inside the channel increase as a result of the chamfering. The strong dependence of the erosion on the effective sputtering yield Y_{osc} render the significance of the C–K short, important in terms of contribution to the total erosion, but benign relative to the importance of the plasma oscillations.

V. Conclusions

Numerical simulations of the partially ionized gas in a discharge hollow cathode have been performed to understand the behavior of the plasma and the associated mechanisms responsible for the erosion of the keeper electrode. The numerical results are the solution to an extensive, 2-D mathematical model of the gas assumed to consist of electrons, singly charged xenon ions, and xenon atoms. In the model, the electrons and ions are assumed to behave as distinct inertia-less fluids. Based on this (fluid) point of view, it is found that the plasma resistivity in the near-plume region of the cathode is effectively enhanced by turbulent fluctuations that are likely the product of ion acoustic instabilities. These conclusions support previous theoretical and empirical work performed in a larger (1.5-cm) discharge cathode. Although the extent to which these instabilities alter the electron energy distribution function is still unclear, it is found that with an effective resistivity model that has been based largely on the time-averaged measurements, the bulk behavior of the plasma properties is reproduced. It is also shown that the conditions in the discharge are sufficient to produce runaway electrons and ion heating, both of which have long been associated with IAT in current-carrying plasmas.

The results from the plasma simulations have been applied to predict the erosion patterns observed in two long-duration life tests of a 30-cm ion thruster. It is found that the plasma fluctuations effectively enhance the average energy with which ions strike the keeper. In turn, the effective sputtering yield of the keeper material is higher in magnitude but exhibits a weaker dependence on the sheath drop. As a result, the nonmonotonic trend of the keeper erosion pattern observed in the Life Demonstration Test is reproduced by the model. Without the ion energy enhancement, the predicted erosion is monotonic with radius and almost 2 orders of magnitude less in magnitude. It is found that if the same amplitude of oscillations A used to predict the erosion of the keeper face is used in the channel interior, the maximum erosion observed at the keeper channel exit is closely reproduced. However, at fixed A, the prediction overestimates the erosion at the entrance to the keeper orifice. Based on the computed classical collision frequencies, it is proposed that the turbulence is reduced upstream of the keeper exit due to damping of the waves. When the erosion calculations are extended to include operation of the cathode at the lower-power level (TH8), it is found that the C–K short that occurred during this time contributed about 2% to the enlargement of the channel, and that the accelerated erosion detected to begin around this time would have occurred regardless of the short but most likely later in the test.

The work presented in this paper exposes several areas of increased complexity, mostly associated with the plasma turbulence and related wear mechanisms, that require further extensive investigations. In regard to keeper life, the results show a strong dependence of the erosion on the amplitude of the oscillations, which can vary with operating conditions and/or location relative to the keeper. An extensive characterization of the turbulent spectrum by both theoretical and empirical means has not yet been performed. The issues of ion heating, electron runaway, and anomalous resistivity have also not been rigorously investigated under typical discharge cathode operating conditions. The implementation of a global anomalous resitivity model allows us to solve a relatively complex mathematical model of the partially ionized gas in these devices by assuming that the bulk electrons are heated by the turbulence. But the precise functional dependencies of the turbulent resistivity in the presence of material surfaces, classical collisions, applied magnetic field, and ion heating remain unknown in these cathodes.

Acknowledgment

The research described in this paper was carried out by the Jet Propulsion Laboratory, California Institute of Technology, under a contract with the National Aeronautics and Space Administration in support of the In-Space Propulsion Technology Program.

References

[1] Polk, J. E., Anderson, J. R., Brophy, J. R., Rawlin, V. K., Patterson, M. J., Sovey, J., and Hamley, J., "An Overview of the Results from an 8200 Hour Wear Test of the NSTAR Ion Thruster," AIAA Paper 99-2446, June 1999.

[2] Sengupta, A., Brophy, J. R., and Goodfellow, K. D., "Status of the Extended Life Test of the Deep Space 1 Flight Spare Ion Engine after 30,352 Hours of Operation," AIAA Paper 03-4558, July 2003.
[3] Kameyama, I., "Effects of Neutral Density on Energetic Ions Produced Near High-Current Hollow Cathodes," NASA CR-204154, Oct. 1997.
[4] Katz, I., Mikellides, I. G., Goebel, D. M., Jameson, K. K., Wirz, R., and Johnson, L. K., "Production of High Energy Ions Near an Ion Thruster Discharge Hollow Cathode," AIAA Paper 06-4485, July 2006.
[5] Gallimore, A. D., Rovey, J. L., and Herman, D. A., "Erosion Processes of the Discharge Cathode Assembly of Ring-Cusp Gridded Ion Thrusters," *Journal of Propulsion and Power*, Vol. 23, No. 6, 2007, pp. 1271–1278.
doi:10.2514/1.27897
[6] Williams, G. J., Domonkos, M. T., and Chavez, J. M., "Measurement of Doubly Charged Ions in Ion Thruster Plumes," International Electric Propulsion Conference Paper 01-310, Oct. 2001.
[7] Foster, J. E., and Patterson, M. J., "Downstream Ion Energy Distributions in a Hollow Cathode Ring Cusp Discharge," *Journal of Propulsion and Power*, Vol. 21, No. 1, 2005, pp. 144–151.
doi:10.2514/1.4771
[8] Latham, P. M., Pearce, A. J., and Bond, R. A., "Erosion Processes in the UK-25 Ion Thruster," International Electric Propulsion Conference Paper 91-096, Oct. 1991.
[9] Goebel, D. M., Jameson, K. K., Katz, I., and Mikellides, I. G., "Energetic Ion Production and Electrode Erosion in Hollow Cathode Discharges," International Electric Propulsion Conference Paper 05-269, Oct. 2005.
[10] Salhi, A., and Turchi, P. J., "A First-Principles Model for Orificed Hollow Cathode Operation," AIAA Paper 92-3742, July 1992.
[11] Boyd, I. D., and Crofton, M. W., "Modeling the Plasma Plume of a Hollow Cathode," *Journal of Applied Physics*, Vol. 95, No. 7, 2004, pp. 3285–3296.
doi:10.1063/1.1651333
[12] Goebel, D. M., Jameson, K. K., Watkins, R. M., Katz, I., and Mikellides, I. G., "Hollow Cathode Theory And Experiment, 1: Plasma Characterization Using Fast Miniature Scanning Probes," *Journal of Applied Physics* [online], Vol. 98, No. 11, 2005, p. 113302.
doi:10.1063/1.2135417
[13] Jameson, K. K., Goebel, D. M., and Watkins, R. M., "Hollow Cathode and Keeper-Region Plasma Measurements," AIAA Paper 05-3667, July 2005.
[14] Mikellides, I. G., Katz, I., Goebel, D. M., Polk, J. E., and Jameson, K. K., "Evidence of Non-Classical Plasma Transport in Hollow Cathodes for Electric Propulsion," *Journal of Applied Physics* [online], Vol. 101, No. 6, 2007, p. 063301.
doi:10.1063/1.2710763
[15] Mikellides, I. G., Katz, I., Goebel, D. M., and Polk, J. E., "Hollow Cathode Theory and Experiment, 2: A Two-Dimensional Theoretical Model of the Emitter Region," *Journal of Applied Physics* [online], Vol. 98, No. 11, 2005, p. 113303.
doi:10.1063/1.2135409
[16] Mikellides, I. G., Katz, I., Goebel, D. M., and Polk, J. E., "Theoretical Model of a Hollow Cathode Plasma for the Assessment of Insert and Keeper Lifetimes," AIAA Paper 05-4234, July 2005.
[17] Mikellides, I. G., Katz, I., and Polk, J. E., "Wear Mechanisms in Electron Sources for Ion Propulsion, 1: Neutralizer Hollow Cathode," AIAA Paper 07-5168, July 2007.
[18] Sengupta, A., Anderson, J. R., Brophy, J. R., Kulleck, J., Garner, C. E., DeGroth, K., Karniotis, T., Banks, B., and Walters, P., "The 30,000-Hour Extended-Life Test of the Deep Space 1 Flight Spare Ion Thruster," NASA T/TP 2004-213391, 2004.
[19] Kolasinski, R. D., and Polk, J. E., "Cathode Keeper Orifice Wear Measurements Using Surface Layer Activation," AIAA Paper 2005-3664, July 2005.
[20] Doerner, R. P., Whyte, D. G., and Goebel, D. M., "Sputtering Yield Measurements During Low Energy Xenon Plasma Bombardment," *Journal of Applied Physics*, Vol. 93, No. 9, pp. 5816–5823.
doi:10.1063/1.1566474
[21] Doerner, R. P., "Low-Energy Sputtering Yields of Tungsten and Tantalum," *Journal of Vacuum Science and Technology A (Vacuum, Surfaces, and Films)*, Vol. 23, No. 6, 2005, pp. 1545–1547.
doi:10.1116/1.2110385
[22] Braginskii, S. I., "Transport Processes in Plasmas," *Reviews of Plasma Physics*, Vol. 1, edited by M. A. Leontovich, Consultants Bureau, New York, 1965, pp. 205–311.
[23] Friedly, V., and Wilbur, P., "High Current Hollow Cathode Phenomena," AIAA Paper 90-2587, July 1990.
[24] Guyot, M., and Hollenstein, C., "Experiments on Potential Gradients in a Current-Carrying Plasma, 1: Potential Structures," *Soviet Journal of Atomic Energy*, Vol. 26, No. 6, Nov. 1967.
[25] Bychenkov, V. Y., Silin, V. P., and Uryupin, S. A., "Ion Acoustic Turbulence and Anomalous Transport," *Physics Reports*, Vol. 164, No. 3, 1988, pp. 119–215.
doi:10.1016/0370-1573(90)90122-I
[26] Sagdeev, R. Z., and Galeev, A. A., *Nonlinear Plasma Theory*, Benjamin, New York, 1969, p. 103.
[27] Kadomtsev, B. B., *Plasma Turbulence*, Academic Press, London, 1965.
[28] Dreicer, H., "Electron and Ion Runaway in a Fully Ionized Gas," *Physical Review*, Vol. 115, No. 2, 1959, pp. 238–249.
doi:10.1103/PhysRev.115.238
[29] Tsytovich, V. N., *Lectures on Non-Linear Plasma Kinetics*, Springer–Verlag, New York, 1995, p. 195.
[30] Galeev, A. A., "Collisionless Shocks," *Physics of the Solar-Planetary Environment*, Vol. 1, American Geophysical Union, Washington, D.C., 1976, p. 464.
[31] Zavoiskii, E. K., and Rudakov, L. I., "Turbulent Heating of Plasma," *Soviet Journal of Atomic Energy*, Vol. 23, 1967, pp. 417–431.
[32] Büchner, J., and Elkina, N., "Vlasov Code Simulation of Anomalous Resistivity," *Space Science Reviews*, Vol. 121, Nos. 1–4, 2005, pp. 237–252.
doi:10.1007/s11214-006-6542-6
[33] Volkov, E. D., Perepelkin, N. F., and Suprunenko, V. A., *Collective Phenomena in Current-Carrying Plasma*, Naukova Dumka, Kiev, Ukraine, 1979, p. 86.
[34] Dum, C. T., Chodura, R., and Biskamp, D., "Turbulent Heating and Quenching of the Ion Sound Instability," *Physical Review Letters*, Vol. 32, No. 22, 1974, pp. 1231–1234.
doi:10.1103/PhysRevLett.32.1231
[35] Zavoiskii, E. K., Nedoseev, S. L., and Rudakov, L. I., "Ion Heating in a Turbulent Plasma," *JETP Letters* (English Translation), Vol. 6, Dec. 1967, pp. 367–369.
[36] Honzawa, T., and Kawai, Y., "Ion Heating Caused by Ion Acoustic Waves in an Ion-Streaming Plasma," *Plasma Physics*, Vol. 14, No. 1, 1972, pp. 27–36.
doi:10.1088/0032-1028/14/1/003
[37] Williams, G. J., Smith, T. B., Domonkos, M. T., Shand, K. J., Gallimore, A. D., and Drake, P. R., "Laser Induced Fluorescence Characterization of Ions Emitted From Hollow Cathodes," AIAA Paper 99-2862, June 1999.
[38] Domonkos, M. T., Foster, J. E., and Patterson, M. J., "Investigation of Keeper Erosion in the NSTAR Ion Thruster," International Electric Propulsion Conference Paper 01-308, Oct. 2001.
[39] Bell, E. W., Djuric, N., and Dunn, G. H., "Electron-Impact Ionization of In^+ and Xe^+," *Physical Review A*, Vol. 48, No. 6, 1993, pp. 4286–4291.
doi:10.1103/PhysRevA.48.4286
[40] Kolasinski, R. D., and Polk, J. E., "Characterization of Cathode Keeper Wear by Surface Layer Activation," *Journal of Propulsion and Power*, Vol. 20, No. 6, 2004, pp. 992–999.
doi:10.2514/1.6191
[41] Brophy, J. R., Ganapathi, G. B., Garner, C. E., and Gates, J., "Status of the Dawn Ion Propulsion System," AIAA Paper 04-3433, July 2004.
[42] Herman, D., Soulas, G., and Patterson, M., "Status of the NEXT Ion Thruster Long-Duration Test after 10,100 h and 207 kg Demonstrated," AIAA Paper 2007-5272, July 2007.
[43] Polk, J. E., Marrese, C., Thornber, B., Dang, L., and Johnson, L., "Temperature Distributions in Hollow Cathode Emitters," AIAA Paper 04-4116, July 2004.

A. Gallimore
Associate Editor